RESEARCH ARTICLE

Three-dimensional effects in quasi two-dimensional free surface scalar experiments

**J. M. García de la Cruz · L. Rossi ·
J. C. Vassilicos**

Abstract The disagreement between free surface scalar experiments and the two-dimensional (2D) transport equation is discussed. An effective diffusivity coefficient, κ_{eff}, is introduced and defined as the quotient between variance decay and mean gradient square. In all the experiments performed, κ_{eff} is significantly larger than the scalar diffusivity, κ. Three mechanisms are identified as responsible for the differences between the quasi two-dimensional (Q2D) experiments and the 2D behaviour of a diffusive scalar. These are the vertical velocity gradients, the free surface divergence and the gravity currents induced by the scalar. These mechanisms, which affect the diffusive term in the 2D transport equation for large Péclet number ($Pe \gg 1$), are evaluated for steady and time-dependant laminar flows driven by electromagnetic body forces.

1 Introduction

Mixing is governed by the transport equation,

$$\frac{d\theta(\boldsymbol{r},t)}{dt} + \boldsymbol{u}(\boldsymbol{r},t) \cdot \nabla \theta(\boldsymbol{r},t) = \kappa \nabla^2 \theta(\boldsymbol{r},t), \tag{1}$$

describing the evolution of a scalar field θ, with diffusivity κ, advected by a velocity field $\boldsymbol{u}$ in a domain $\boldsymbol{r}$. The study of the transport equation has been approached in different manners. To experimentally study mixing in vortical and chaotic flows, Q2D free surface regimes are commonly employed (Gouillart et al. 2009; Jana et al. 1994; Jullien 2003; Voth et al. 2002, 2003). Assuming the system is 2D simplifies the acquisition, analysis and description of the scalar and velocity fields. Unfortunately, several authors noticed discrepancies between obtained and expected results using free surface experiments (Jullien 2003; Jullien et al. 2000; Williams et al. 1997). They attributed the differences to vertical velocity gradients and free surface divergence. Quantifications of these effects or a procedure to evaluate them was not proposed. This manuscript analyses the errors produced by the Q2D assumption in free surface experiments and discusses the framework in which such experiments provide useful information in the study of mixing.

1.1 2D experiments in a 3D world

Free surface scalar experiments are typically performed by recording either the light absorption (Cenedesse and Dalziel 1998) or fluorescent emission (Gouillart et al. 2009; Jullien et al. 2000; Rothstein et al. 1999; Voth et al. 2002) of a thin scalar layer floating on a fluid. The velocity field at the free surface is also acquired when required (Williams et al. 1997). The typical data obtained in Q2D free surface scalar experiments are the fluid free surface velocity and the vertical integral of the scalar concentration along the intersection between laser and fluid. These two fields cover a 2D domain. Whether the acquired 2D concentration field is expected to behave as the transport equation predicts, according to the 2D velocity field obtained, can be answered by comparing the 3D and 2D versions of the transport equation (z being vertical and contrary to the gravity):

J. M. García de la Cruz (✉) · J. C. Vassilicos
Imperial College London, South Kensington Campus,
London SW7 2AZ, UK
e-mail: marcos@imperial.ac.uk

L. Rossi
DEN/DANS/DM2S/LIEFT, CEA Saclay,
91191 Gif-sur-Yvette Cedex, France

$$\frac{\mathrm{d}\theta}{\mathrm{d}t} + u\frac{\partial\theta}{\partial x} + v\frac{\partial\theta}{\partial y} + w\frac{\partial\theta}{\partial z} = \kappa\left(\frac{\partial^2\theta}{\partial x^2} + \frac{\partial^2\theta}{\partial y^2} + \frac{\partial^2\theta}{\partial z^2}\right), \qquad (2)$$

$$\frac{\mathrm{d}\theta}{\mathrm{d}t} + u\frac{\partial\theta}{\partial x} + v\frac{\partial\theta}{\partial y} = \kappa\left(\frac{\partial^2\theta}{\partial x^2} + \frac{\partial^2\theta}{\partial y^2}\right); \qquad (3)$$

where, in Eq. 2, θ, u, v and w are functions of x, y, z and t while, in Eq. 3, θ, u and v are functions only of x, y and t.

The typical Q2D data acquired (for a laser covering the entire fluid depth H) are

$$\theta_Z(x,y,t) = \int_0^H \theta(x,y,z,t)\mathrm{d}z \quad \text{and}$$

$$\boldsymbol{u}_H(x,y,t) = (u(x,y,H,t), v(x,y,H,t)),$$

The 2D statistics are generated from the 2D variables $\boldsymbol{u}_H$ and θ_Z. θ_Z is now a "2D concentration" with units of mass l^{-2}. Writing the horizontal components of the velocity as $u^{1,2}(x,y,z,t) = u_H^{1,2}(x,y,t)(1 - f^{1,2}(x,y,z,t))$ and assuming impermeable fluid boundaries, a vertical integration of Eq. 2 leads to

$$\frac{\mathrm{d}\theta_Z}{\mathrm{d}t} + \boldsymbol{u}_H \cdot \nabla\theta_Z = \kappa\Delta\theta_Z(1 + \varepsilon_H + \varepsilon_w),$$

$$\varepsilon_H = \frac{\boldsymbol{u}_H}{\kappa\Delta\theta_Z}\int_0^H \boldsymbol{f}\cdot\nabla_{2D}\theta\mathrm{d}z, \qquad (4)$$

$$\varepsilon_w = \frac{\int_0^H w\frac{\partial\theta}{\partial z}\mathrm{d}z}{\kappa\Delta\theta_Z} \approx \frac{-\int_0^H \theta\nabla\boldsymbol{u}_H\mathrm{d}z}{\kappa\Delta\theta_Z};$$

where $\nabla\boldsymbol{u}_H$ is the 2D divergence of $\boldsymbol{u}_H$, $\nabla\theta_Z$ and $\Delta\theta_Z$ are the 2D gradient and Laplacian of θ_Z and $\nabla_{2D}\theta$ is the horizontal gradient of θ. Equations 3 and 4 describe the 2D scalar transport and the vertical integration of the 3D scalar transport and only differ in the errors ε_H and ε_w. These errors represent the apparent diffusion produced by vertical gradients and free surface divergence of the velocity field and include all the 3D effects of the flow field generated not only by the electromagnetic forcing but also by other forces affecting the brine motion, such as buoyancy forces, usually difficult to evaluate independently.

The integration of 3D flows affect both, 2D scalar diffusion and advection. Nevertheless, in most of the free surface mixing experiments, advection transports much more scalar than diffusion ($Pe = UL/\kappa \gg 1$), and therefore, diffusion is the most strongly affected term. As a result, these 3D effects are compared with diffusion instead of advection in Eq. 4.

1.2 Passive scalars and gravity currents

"A passive scalar is a diffusive contaminant in a fluid flow that is present in such low concentration that it has no dynamical effect (such as buoyancy) on the fluid motion itself" (Warhaft 2000). Transport experiments are commonly

based on the inclusion of a passive scalar in a flow. The evolution of such a scalar is then governed by the transport equation. The matter remains in defining how innocuous the added scalar needs to be, for its presence not to affect the flow so much as to appreciably modify the statistics with respect to those obtained using an actual passive scalar. Small density differences produce gravity currents that affect the velocity field. When a scalar is injected in a 3D flow, the convection is effectively compared with the advection, usually orders of magnitude higher, and the scalar can fairly be considered passive. Nevertheless, when the experiments are meant to be Q2D, gravity currents coherently affect the flow two-dimensionality. If $Pe \gg 1$, gravity currents must be compared with diffusion, usually extremely low. As a result, a baroclinic flow, negligible for 3D scalar statistics, can be decisive in Q2D experiments. Even if the effect of gravity currents could be included in ε_w, we prefer to isolate the free surface divergence genuine of the velocity field, which is constant in time and has its own dynamics, from the effect of gravity currents, which depends on the characteristics of the scalar and its effect fades down with time, as the dye levels with the brine free surface.

1.3 Objectives

With the three mechanisms identified as possibly affecting the free surface experiments, the expected Q2D transport equation finally reads

$$\frac{\mathrm{d}\theta_Z}{\mathrm{d}t} + \boldsymbol{u}_H \cdot \nabla\theta_Z = \kappa\Delta\theta_Z\big(1 + \varepsilon_H + \varepsilon_w + \varepsilon_{\mathrm{gc}}\big), \qquad (5)$$

where $\varepsilon_{\mathrm{gc}}$ is the apparent diffusion produced by gravity currents divided by the 2D diffusion.

Multiplying the 2D transport equation (Eq. 3) by θ and integrating in an impermeable space with a divergence free velocity field lead to

$$\frac{\mathrm{d}\langle\theta^2\rangle}{\mathrm{d}t} = -2\kappa\big\langle|\nabla\theta|^2\big\rangle. \qquad (6)$$

Analogously for the Q2D case, we can write

$$\frac{\mathrm{d}\langle\theta_Z^2\rangle}{\mathrm{d}t} = -2\kappa_{\mathrm{eff}}\big\langle|\nabla\theta_Z|^2\big\rangle,$$
$$\frac{\kappa_{\mathrm{eff}}}{\kappa} = \left(1 + \frac{\kappa_H}{\kappa} + \frac{\kappa_w}{\kappa} + \frac{\kappa_{\mathrm{gc}}}{\kappa}\right); \qquad (7)$$

where κ_H, κ_w and κ_{gc} are the excess over the expected 2D diffusivity produced by horizontal velocity gradients, free surface divergence and gravity currents. In order to evaluate κ_{eff}, the variance decay rate and the mean gradient squared are measured, making

$$\frac{\kappa_{\mathrm{eff}}}{\kappa} = \left(\frac{\mathrm{d}\langle\theta_Z'^2\rangle}{\mathrm{d}t}\right)\Big/\left(-2\kappa\big\langle|\nabla\theta_Z|^2\big\rangle\right) \qquad (8)$$

It can be noted that this measure will be affected by the acquisition system resolution if the scalar has length scales shorter than the size projected by a camera pixel.

In the rest of the text, only the vertical integral of concentration θ_Z will appear, since it is the only concentration that could be measured with the apparatus described. In order to simplify the notation, θ_Z will be called from now simply θ, but will still represent a "2D concentration".

2 Apparatus and experimental procedure

The experiments were performed over a forced shallow layer of fluid. The velocity field was acquired using particle image velocimetry (PIV). The decaying scalar field, obtained labelling the fluid with a blob of dye, was acquired using laser-induced fluorescence. Further details of the apparatus and procedure can be accessed in Garcia de la Cruz (2011).

2.1 Laboratory apparatus

To generate the flows which stir the scalar, a shallow layer of a conductive solution of NaCl was electromagnetically forced by an ionic current and a pair of magnets, as presented on the left-hand side of Fig. 1. The wall supporting the brine is a rectangle of dimensions 500×600 mm^2 and thickness 1 mm. The area recorded is a square, centred in that rectangle, of side 440 mm. The brine free surface extends up to a square of side 600 mm. The brine nominal depth employed is 6 mm, measured with a 10 μm resolution micrometre, and it varied in less than 0.05 mm during one experiment. The wall flatness and horizontality are characterized by measuring its distance to the brine free surface in a mesh of 4×4 nodes: the maximum difference and standard deviation of these readings are respectively kept smaller than 7 and 4 % of the fluid depth.

The measurements area was recorded with a progressive scan camera (14 Bit), model Imager Pro Plus 4M CCD. The resolution of the CCD is $2{,}048 \times 2{,}048$ pixels. The maximum frequency is 14 Hz. The size projected by one pixel is 440 mm/2,048 ≈ 0.215 mm.

The laser employed for LIF is a Nd:YAG laser which provides 200 mJ in the wavelength of 532 nm for a pulse width around 4 ns. The laser, expanded in a cone, homogeneously and perpendicularly illuminates the measurements area, around 2 m away.

Similarly to Rossi et al. (2006), the magnetic field is generated by a pair of cubic magnets of edge 40 mm, with a magnetic intensity around 0.3 T, placed 40 mm apart and in contact with the wall bottom. The magnetic field is closed under the magnets by an iron bar. The centre of the pair of magnets is fixed and centred with the recording area. The attitude of the magnet pair, whose angle is defined on the right-hand side of Fig. 1, is automatically operated during the experiment and positioned with an accuracy of $\pm 0.7°$.

The ionic current is driven by a voltage between two arrays of twenty electrodes homogeneously distributed along 600 mm. Each electrode is made by a 30 mm, 99.95 % platinum wire of diameter 250 μm. The ionic current is regulated through a circuit which maintains its relative standard deviation lower than 0.5 %.

When brine stratification is required, fresh water is added by a regular distribution of 113 injectors separated around 56.6 mm. The relative standard deviation of the stratification thickness decreases with time, and after 30 s, it is smaller than 1 %.

In the scalar experiments, the dye is smoothly placed at the brine top using a 6 mm calibre injector. The flow rate is controlled by a syringe pump *Model '11' Plus, HARVARD APPARATUS*. The maximum flow rate for the dye not to sink down to the wall, around $1\,\mathrm{ml\,s}^{-1}$, was employed by default to ensure a minimal interference between brine motion and scalar initial condition.

All the liquids employed in the experiments (salt water, fresh water and RH6G) were prepared the day before and left overnight to acclimatize with the room. The temperature of the room during the experiments oscillated between 18 and 21 °C but never changed in more than 2 °C during any day or more than 0.1 °C during any experiment.

2.2 Velocity field acquisition

The free surface velocity fields were acquired using PIV (Raffel et al. 1998) in free surface flows (Voth et al. 2002, 2003; Williams et al. 1997). Particles of PLIOLITE DF01 with a diameter between 100 and 200 μm, floating at the free surface and advected by it, were employed as seeding. The brine used in the velocity field acquisition was a solution of NaCl in water at $160\,\mathrm{g\,l}^{-1}$, with a density of $1{,}120\,\mathrm{kg\,m}^{-3}$, a viscosity of $10^{-6}\,\mathrm{m}^2\,\mathrm{s}^{-1}$ and a conductivity of $170\,\mathrm{mS\,cm}^{-1}$ (Weast 1989; Wolf 1966). The velocity fields were obtained in a regular mesh of 222×222 windows with an overlap of 50 % and covering an area of $\sim 380 \times 380\,\mathrm{mm}^2$ (the distance between nodes is more
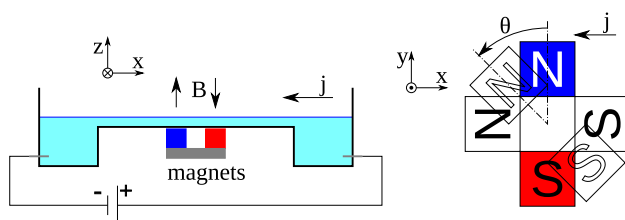
Fig. 1 Electromagnetic tank and magnet positioning

than 20 times smaller than a magnet). The in-house PIV software employed has an uncertainty smaller than $0.2\,\text{pix frames}^{-1}$ (Rossi et al. 2009).

2.3 Scalar field acquisition

Laser-induced fluorescence (LIF) is employed to acquire the scalar field, a solution of Rhodamine 6G (Rh6G) with a diffusivity, κ, around $1.2 \times 10^{-4}\,\text{mm}^2\,\text{s}^{-1}$ (Axelrod et al. 1976). The LIF measurement method is based on the immediate light emission that fluorescent substances present to a luminous excitation (Guilbault 1973). The absorption and emission peaks of the Rh6G are respectively located at 530 and 552 nm. A 540-nm-long pass filter covered the camera lens during the LIF experiments. This prevents the light directly emitted by the laser to access the CCD while recording most of the light emitted by the dye.

The fluorescence F is proportional to the exciting intensity, I_0, and varies exponentially with the dye concentration, c, the compound absorptivity, ϵ, and the cell path length, b, as $F \propto I_0\left(1 - e^{-\epsilon b c}\right)$. In the experiments performed, $b < 1\,\text{cm}$ and $\epsilon < 10^5\,\text{cm}^{-1}\,\text{M}^{-1}$, and therefore, the linear behaviour,

$$F \propto I_0 b c, \tag{9}$$

is expected up to concentrations of $c \approx 10^{-5}\,\text{M}$.

2.3.1 LIF calibration

The raw LIF data are calibrated to provide the dye acquired by each pixel independently of the heterogeneities produced by the acquisition system. To perform the spatial calibration the light emitted by several depths of homogeneous Rh6G at a reference concentration, c_{ref}, is acquired. In each realization, the total depth is conceptually split in a homogeneous layer of constant height b, over a horizontal plane under which a layer of dye, $b_0(x, y)$, contains the wall irregularities. From Eq. 9, the light projected in each pixel is

$$F(x, y) \propto (I_0(x, y)b_0(x, y) + I_0(x, y)b)c_{\text{ref}}. \tag{10}$$

After acquiring several thicknesses, $I_0(x, y)$ is found in each pixel using a least squared error fit relating $F(x, y)$ and b. The mass of dye in each pixel, $c(x, y)$, is obtained by subtracting the background (previously recorded for each experiment), $B(x, y)$, and dividing the result by $I_0(x, y)$, as

$$c(x, y) = \frac{F(x, y) - B(x, y)}{I_0(x, y)}. \tag{11}$$

To perform the calibration, around 1 mm of Rh6G at $6.2 \times 10^{-7}\,\text{M}$ was recurrently added (14 times) to the acquisition

area from a minimum depth ($\sim 3\,\text{mm}$), limited by surface tension, to the maximum depth before the camera saturates ($\sim 16\,\text{mm}$). For each addition, the same process is repeated five times: the total depth is measured with a micrometre; the dye is energetically stirred; 51 pictures are taken. It was verified that the scattering produced by the acquisition system was more than one order of magnitude larger than that produced by dye heterogeneities. More than 98 % of the pixels presented a coefficient of determination (R^2) above 0.999 when adjusted by the Eq. 9.

The improvement obtained by calibrating a randomly chosen picture with an expected homogeneous distribution of dye is shown in Fig. 2. The power spectra of a homogeneous field before and after the calibration using single picture statistics (SPS) show a strong error reduction for wavelengths smaller than $10^{-2}\,\text{mm}^{-1}$ and between 10^{-1} and $10^0\,\text{mm}^{-1}$. The relative standard deviation changed from 22 to 6 %.

The spatial calibration only reduces the acquisition system errors which are coherent in time and it does not affect its temporal oscillations, called from now on *acquisition system noise* (ASN). The ASN was measured around 5 % of the measured light. The ASN presented spatial coherent structures, highly correlated at distances under 20 mm. Adjacent pixels presented a binormal distribution of the ASN. A temporal analysis showed a Gaussian time delta correlated distribution of the ASN.

2.3.2 LIF estimators

The scalar power spectrum is obtained through a specifically designed estimator which reduces the uncertainty for the particular ASN.
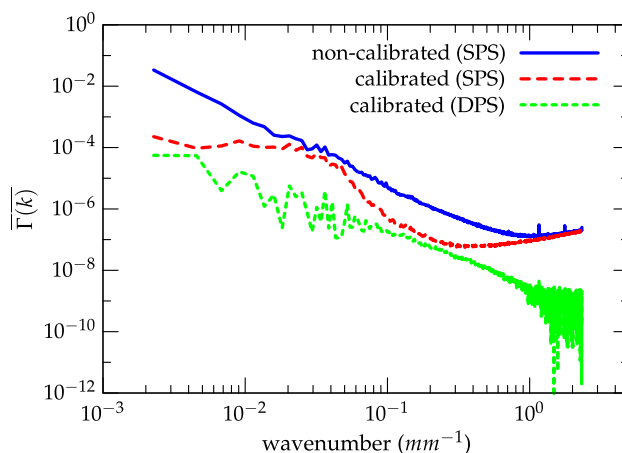
Fig. 2 Example of calibration. Power spectra of uncalibrated and calibrated homogeneous fields normalized with their average using single (SPS) and double picture statistics (DPS)

After the spatial calibration, we can assume that the expected amount of light captured by a pixel i in each picture j is homogeneously proportional to the mass of dye projected in that pixel. The noise affecting this value has a delta correlated in time normal distribution and is highly correlated with its neighbours with a binormal distribution. In our set up, the standard deviation of such normal distributions is approximately 0.05 times its expected value. Each reading, c, can be approximated by

$$c_i^j \approx N_i^j(\mu_i^j, \sigma_i^j(\mu_i^j)) \approx \mu_i^j(1 + \sigma \mathcal{N}_i^j), \qquad (12)$$

where μ_i^j is the mass of dye projected in the pixel, $\mathcal{N}_i^j$ is the random variable corresponding to the ASN, with average 0 and variance 1, and σ is the proportionality constant between μ_i^j and the standard deviation σ_i^j.

Assuming a multinormal distribution of the noise for all the pixels, each spectral node also follows a normal distribution with a mean equal to the actual value of the Fourier component described by

$$C_i^j \approx \mathcal{N}_i^j(M_i^j, \Sigma_i^j) = M_i^j + \Sigma_i^j \mathcal{N}_i^j, \qquad (13)$$

where C_i^j and M_i^j are the Fourier components of c^j and μ^j in node i and Σ_i^j is its standard deviation, which depends on all the pixels and their correlations. Although multinormality is a reasonable hypothesis in view of the data, it has not been evidenced and the results should be adequately validated in each case.

To obtain the scalar spectrum for the spectral statistical distribution presented in Eq. 13, each sample is acquired as a pair of pictures, A and B. Each pair should be recorded within a time short enough to assume a constant scalar pattern. Due to its temporal delta correlation, the noise will completely change between the two pictures of any pair. The estimator employed to obtain the scalar energy contained in the wavenumber k is:

$$Z_{\Gamma(k)} = \sum_{k \le r(i) < k+1} \left(C_{R,i}^A C_{R,i}^B + C_{I,i}^A C_{I,i}^B \right), \qquad (14)$$

where R and I refer to real and imaginary and the summation includes those nodes with a wavenumber modulus $\sim k$. The expected value of this estimator is:

$$E[Z_{\Gamma(k)}] = \sum_{k \le r(i) < k+1} \left(M_{R,i}^A M_{R,i}^B + M_{I,i}^A M_{I,i}^B \right). \qquad (15)$$

As noticed, the estimator employed in the double picture statistics (DPS) is, assuming the spectral distribution as presented in Eq. 13, unbiased. This is unlike the classical estimators employed in single picture statistics (SPS), Williams et al. (1997), which square a single picture, converting the unbiased normal ASN into a nonzero-mean chi-squared distribution.

The expected value of the DPS is closer to the actual value the more similar are the scalar distributions of the two frames of the pair. In the experiments reported here, the time delay between the pictures of a pair was 100 ms. An upper bound of the flow velocity employed is 7 mm s^{-1}. Therefore, the DPS measure scalar perturbations down to wavelengths of the order of 0.7 mm. This threshold is nevertheless effectively reduced because the root-mean-squared (r.m.s.) velocity in the relevant central area of the domain (circular region of diameter 200 mm, 5 times the magnet size) is one order of magnitude smaller than the maximum. Therefore, in most of the experimental area, scalar incoherences only occur at wavenumbers beyond the camera resolution ($\sim$0.245 mm).

The benefits of the DPS in the scalar spectrum are illustrated in Fig. 2. To provide a fair comparison, the samples in the SPS are built from an average between the two pictures employed in the DPS. The DPS strongly reduce the ASN at low (10^{-2} to 10^{-1} mm^{-1}) and high (>0.5 mm^{-1}) wavenumbers, presumably where the laser and camera oscillations have a stronger presence. This range for maximum reduction of the ASN by the DPS complements the improvement achieved by the spatial calibration. The integral and second moment of the scalar power spectrum (i.e. variance and mean gradient squared) in the SPS are respectively almost 3 and 30 times larger than in the DPS for a uniform field.

2.3.3 Temporal derivatives

The first temporal derivative of the variance is obtained as the slope of a first-order polynomial adjusted by a least square error method to 25 samples (12.5 s, less than one quarter of the minimum timescale expected) centred in the desired time step.

3 Scalar spreading and diffusing in a quiescent fluid

According to Eq. 1, the expected evolution of the length scale of a blob of dye diffusing in quiescent fluid is $\ell \sim \sqrt{\kappa t}$. This section evaluates the distortion of the Q2D transport equation produced by gravity currents in homogeneous and stratified brine.

3.1 Homogeneous brine

A simple model of the dye spreading in homogeneous brine can be built assuming that the lighter fluid maintains its properties, spreading as a vertical cylinder with constant volume (Hoult 1972). The main parameters employed to describe such a system are presented in Fig. 3. The cylinder
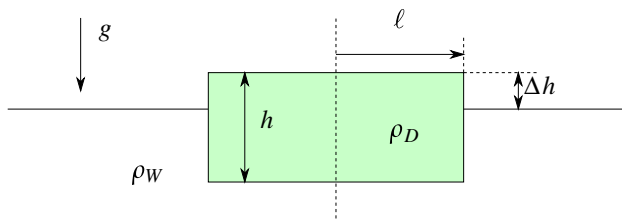
Fig. 3 Homogeneous spreading. Geometry employed to model gravity currents on a blob of dye released in homogeneous brine

Table 1 Homogeneous brine experimental parameter variation

NaCl (g l^{-1})	$\Delta \times 10^3$	Rh6G (ml)	inj. (ml s^{-1})
2.5	1.99	1	0.25
5	3.96	0.5	0.25
5	3.96	1	0.25
5	3.96	1.5	0.25
5	3.96	2	0.25
10	7.86	1	0.25
20	15.44	1	0.25
40	29.85	1	0.25
80	55.94	1	0.12
80	55.94	1	0.25
80	55.94	1	0.50
80	55.94	1	1.00

Values of the parameters varied (brine concentration, Δ, volume of dye injected and injection speed) for the homogeneous brine spreading characterization

modelling the blob of dye has a base of length ℓ and a depth h. The total volume of dye is $V \sim h\ell^n$, with $n = 1$ for 2D and $n = 2$ for 3D spreading. The relative difference of densities between dye, ρ_D, and water, ρ_W, is measured by $\Delta = 1 - \rho_D/\rho_W$.

The procedure followed to scale the gravitational spreading is based on a box-model, originally proposed in Fay (1969) and often followed in literature (Fay 1971; Hoult 1972). In this, the motion of the spreading bulk of lighter fluid results as a balance in time, t, between the gravitational, inertial and viscous forces:

$$F_P \sim \rho_W g h^2 \Delta \ell^{n-1}, \tag{16}$$

$$F_I \sim \rho_D h \ell^{n+1} t^{-2}, \tag{17}$$

$$F_V \sim \delta^{-1} \rho_W \nu_W \ell^{n+1} t^{-1}; \tag{18}$$

The pressure force, F_P, is produced by the gravity g and the height difference in the free surfaces. The inertia force, F_I, is related with the mass of the dye. Finally, the viscous force, F_V, comes from the effect of the viscosity, ν_W, along the boundary layer thickness, δ. Individually balancing the pressure force, which is the only driving term, with the inertia or viscous forces leads to the spreading regimes

$$\text{Inertial spreading} \rightarrow \ell \sim (g\Delta V t^2)^{\frac{1}{n+2}}, \tag{19}$$

$$\text{Viscous spreading} \rightarrow \ell \sim (\nu^{-\frac{1}{2}} g \Delta V^2 t^{\frac{3}{2}})^{\frac{1}{2n+2}}. \tag{20}$$

Each regime governs the spreading when its associated restraining force is stronger: the motion is first inertial and subsequently viscous. The characteristic time between these regimes is the one for which both forces are equal, $t_c \sim (\Delta g)^{-\frac{2n}{5n+2}} V^{\frac{4}{5n+2}} \nu^{-\frac{n+2}{5n+2}}$ (Hoult 1972).

The accuracy of the model presented is tested to evidence the relevance of gravity currents in Q2D free surface experiments in homogeneous brine. To that end, the evolution of several blobs of dye spreading on brine is recorded, varying the brine concentration, volume of dye and injection speed, as summarized in Table 1.

An estimation of t_c can be performed knowing the values of V and Δ employed and using a gravity of $10^4 \, \text{mm s}^{-2}$ and a water viscosity of $1 \, \text{mm}^2 \, \text{s}^{-1}$. The

maximum and minimum t_c expected are around 10 and 1 s. Due to the delay between the injection and the acquisition start, only the viscous regime was clearly captured in the experiments.

Figure 4 presents the evolution of the 2D variance of the concentration normalized with its average for two configurations. The 2D normalized variance of the gravitational spreading model presented in Fig. 3, scales as $\overline{\theta^2}/\overline{\theta}^2 \sim \overline{\theta^2}/V^2 \sim \ell^n h^2 V^{-2} \sim \ell^{-n}$. The expected $\overline{\theta^2}/\overline{\theta}^2$ for 3D spreading or diffusing is

$$\text{3D Inertial spread} \rightarrow \overline{\theta^2}/\overline{\theta}^2 \sim (g\Delta V)^{-\frac{1}{2}} t^{-1}, \tag{21}$$

$$\text{3D Viscous spread} \rightarrow \overline{\theta^2}/\overline{\theta}^2 \sim (\nu^{-\frac{1}{2}} g\Delta V^2)^{-\frac{1}{3}} t^{-\frac{1}{2}}, \tag{22}$$

$$\text{3D Diffusion} \rightarrow \overline{\theta^2}/\overline{\theta}^2 \sim (\kappa t)^{-1}. \tag{23}$$

According to Eq. 22, the expected time exponent for $\overline{\theta^2}/\overline{\theta}^2$ in viscous spreading should be -0.5, unlike in the expected diffusive case, Eq. 22, where it should be -1. The average of the exponents obtained fitting power laws to the acquired data (with R^2 always above 0.98) is -0.44. These exponents do not seem to be related with V, Δ or the injecting speed.

The influence of V, Δ and the injection speed over σ'^{2*} was evidenced by fitting power laws at each time step to the variation that these parameters produced over σ'^{2*}. It was observed that the exponents of V and Δ (with R^2 always above 0.9) asymptotically approached to the expected $-2/3$ and $-1/3$ with an error in both cases smaller than 5 % after 2,000 s. The injection speed nevertheless did not present a clear power law.
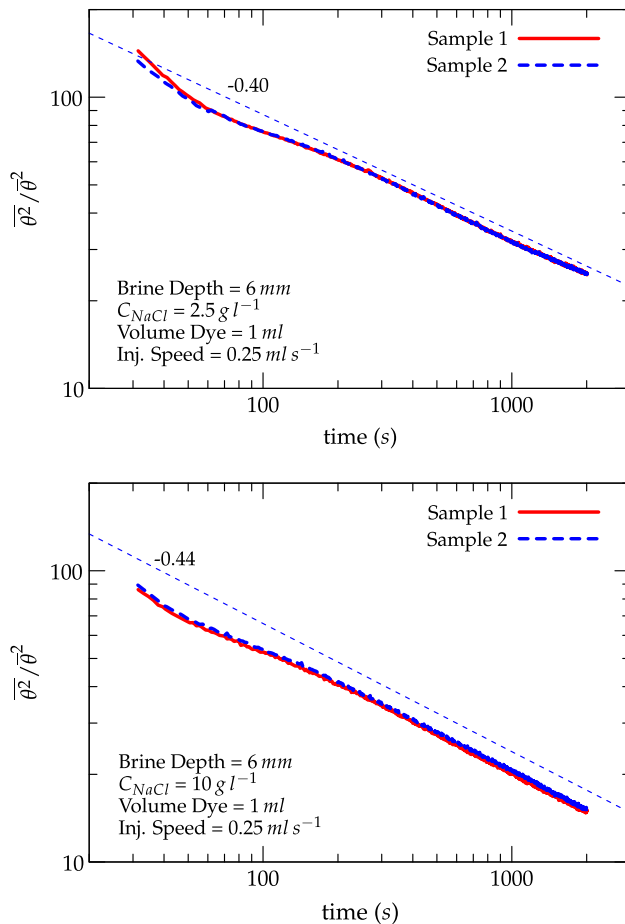
Fig. 4 Gravity current induced 2D variance decay in homogeneous brine. Variance evolution in two samples for two configurations in homogeneous brine gravity currents

3.2 Stratified brine

Brine stratification is employed in free surface scalar experiments because it maintains the scalar away from the strong velocity gradients near the brine bottom, with a higher strength than the expected for a homogeneous brine producing the equivalent gravity currents at the top. The complexity of gravity currents in stratified fluids is such that even the simplest models depend on many parameters difficult to evaluate (Amen and Maxworthy 1980; Ungarish and Huppert 2004; Wu 1969). Accurately, modelling gravity currents in stratified media is beyond the scope of this paper. Instead, it is intended to evidence their existence in Q2D scalar experiments and evaluate their relevance.

The initial stratification law employed here is close to a thin layer of freshwater (~ 0.5 mm) homogeneously distributed over a shallow layer of brine (~ 5 mm) with the selected NaCl concentration. After the dye injection, the NaCl diffuses through the freshwater and dye as a whole

with $\kappa_{\mathrm{NaCl}} \sim 10^{-3}$ mm^2 s^{-1}. The time elapsed from stratification to dye injection, t_{si}, varies the vertical distribution of the brine density under which the dye spreads. In this process, there are two timescales: the time for the NaCl to diffuse through the freshwater, $t_1 \sim \ell^2/\kappa = (0.5\,\mathrm{mm})^2/(10^{-3}\,\mathrm{mm}^2\,\mathrm{s}^{-1}) \sim 4$ min, and the time for the entire brine to become homogeneous, $t_2 \sim 400$ min. Before t_1 there is a thin layer of freshwater at the brine top and the injected dye spreads at that depth with its equal density. At $t_1 < t < t_2$, the entire brine is more dense than the dye, and this will spread at the brine top similarly to the homogeneous case, which will be recovered after t_2. To study the effect of t_{si}, 1 ml of dye was injected at 1 ml s^{-1} after waiting 1, 1.5, 2, 4 or 8 min from homogeneously stratifying 5.6 mm of a NaCl solution at 80 g l^{-1} with 0.4 mm of freshwater.

Two samples taken for one configuration are shown in Fig. 5 top. As observed, a power law is also a good approximation for the variance decay produced by gravitational spreading in stratified media. The influence of t_{si} in the exponent of that power law is presented in Fig. 5 bottom. As shown, the NaCl diffusion before injection gradually reduces the effect of stratification in the gravitational spreading.

The effect of the freshwater layer depth was measured by varying it to 0.5 or 0.25 mm, using enough NaCl solution to obtain a total brine depth of 6 mm and $t_{\mathrm{si}} = 1$ min. The influence of the NaCl concentration was studied by using 5.6 mm of brine at 10 g l^{-1} and 0.4 mm of freshwater, and $t_{\mathrm{si}} = 4$ min. The results (not plotted) showed that the absolute value of the time exponent increased with the brine concentration (unlike the homogeneous brine spreading) and decreased with the fresh layer depth.

3.3 Effective diffusivity in unforced flows

In unforced flows, the excess over 1 of $\kappa_{\mathrm{eff}}/\kappa$ is the relative error associated with the effect that solely gravity currents produce on the Q2D transport equation. Figure 6 presents the evolution of $\kappa_{\mathrm{eff}}/\kappa = (1 + \kappa_{\mathrm{gc}}/\kappa)$, obtained using Eq. 8. In homogeneous brine, as the NaCl concentration is reduced, the initial value of $\kappa_{\mathrm{eff}}/\kappa$ diminishes but, for large times, all the concentrations tested collapse. Brine stratification reduces the value of $\kappa_{\mathrm{eff}}/\kappa$; as t_{si} increases, the curves smoothly tend to the homogeneous case. In all the configurations tested, gravity currents dominate the variance decay during the entire experiment: although $\kappa_{\mathrm{eff}}/\kappa$ diminishes with time, it never reaches constant value, and after 2,000 s, the smallest κ_{eff} measured is two orders of magnitude larger than κ.
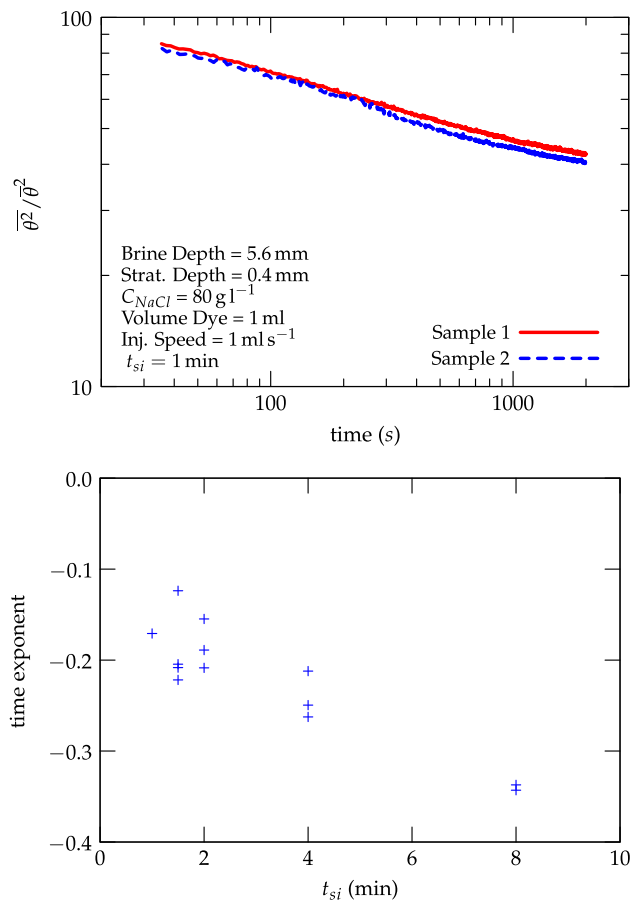
Fig. 5 Gravity current induced 2D variance decay in heterogeneous brine. *T*op graph presents the variance evolution in two samples of the same configuration for heterogeneous brine gravity currents. *B*ottom graph shows the time exponent dependence of a power law fitting the variance decay with the time elapsed between stratification and injection, t_{si}

4 Scalar spreading and diffusing while advected by a Q2D flow

This section analyses a scalar spreading and diffusing while advected by an electromagnetically forced flow. The experiments were performed injecting 1 ml of Rh6G 1.5 min after the stratification of 5.6 mm of NaCl at $80\,\mathrm{g\,l^{-1}}$ with 0.4 mm of fresh water.

4.1 Velocity field characterization

The velocity fields stirring the scalar are either steadily forced, where the magnetic field is maintained constant, or unsteadily forced, where the magnetic field is switched (at $0.25\,\mathrm{rev\,s^{-1}}$) between two steady positions with a pre-established frequency. The flows selected for the scalar experiments are obtained at magnet angles 0°, 15°, 90° and 345°. These flows are presented in Fig. 7, with the exception of the magnet angle 345°, whose topology is
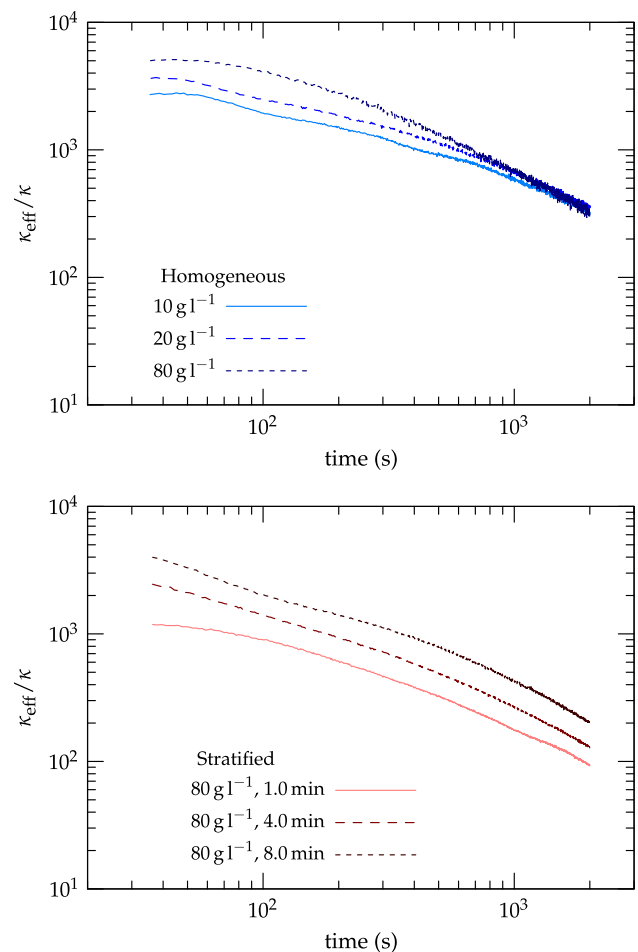
Fig. 6 Effective Q2D diffusivity. Evolution of the ratio $\kappa_{\mathrm{eff}}/\kappa$ for a blob of dye spreading in homogeneous and stratified brine with different concentrations and t_{si}
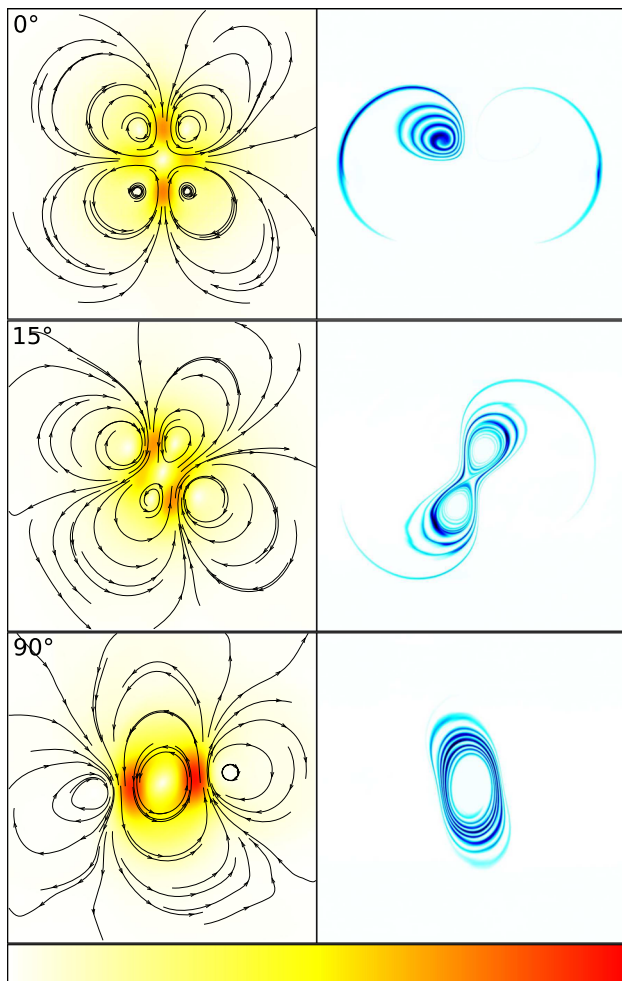
symmetric with respect to the obtained at 15°. The flow unsteadiness, measured by the spatial r.m.s. of the velocity temporal standard deviation, was always smaller than 5 % of the average velocity spatial r.m.s. for steady forcing.

The unsteady forcing configurations were obtained by switching the magnet angle between 0° and 90° with periods 50, 100 or 200 s and between 15° and 345° with a period of 100 s. Each period of the unsteady velocity fields therefore consists of two steady intervals linked by a transient, whose duration scales with the brine depth, h, and kinematic viscosity, v, as $t \sim h^2/v \sim 30\,\mathrm{s}$. Hence, transients take only a small part of the configuration with period 200 s, and their relative relevance increases as the period reduces. The shortest period, 50 s, never reaches the steady state.

4.2 Scalar initial condition

The statistics over a homogeneous distribution of initial conditions were considered. To determine the minimum

developed by the scalar enhances gravity currents. Also, ε_w and ε_H may have a relevant effect.

The evolution of $\kappa_{\mathrm{eff}}/\kappa$ for two samples in a steady and an unsteady configuration is presented in Fig. 8. As the dye homogenizes, the temporal derivatives become noisier relative to the concentration gradients and larger fluctuations in this variable are observed. In the experiments performed, this effect was more pronounced in the steady cases since the unsteady flows lead to chaotic patterns with a more uniform concentration, which reduces the effect of the noise in the spatial average. In spite of this, two ranges can be clearly identified in all the samples tested, independently of the initial condition and flow configuration. The initial regime, which usually lasts between 100 and 300 s, is a steep decay. The second regime is nearly a constant and lasts for the rest of the experiment (around 1,000 s) with no evidence suggesting that it may change later. To study the behaviour of κ_{eff}, the value of its

Fig. 7 Velocity fields in forced experiments. Flows obtained with 6 mm of brine and 24 mA at magnet angles 0°, 15° and 90°, and examples of the scalar pattern that they produce, obtained using the procedure described in Sect. 2.3. The frame size is 382 mm. The velocity scale range is $|\boldsymbol{u}| \subset [0, 7.0]\,\mathrm{mm\,s^{-1}}$
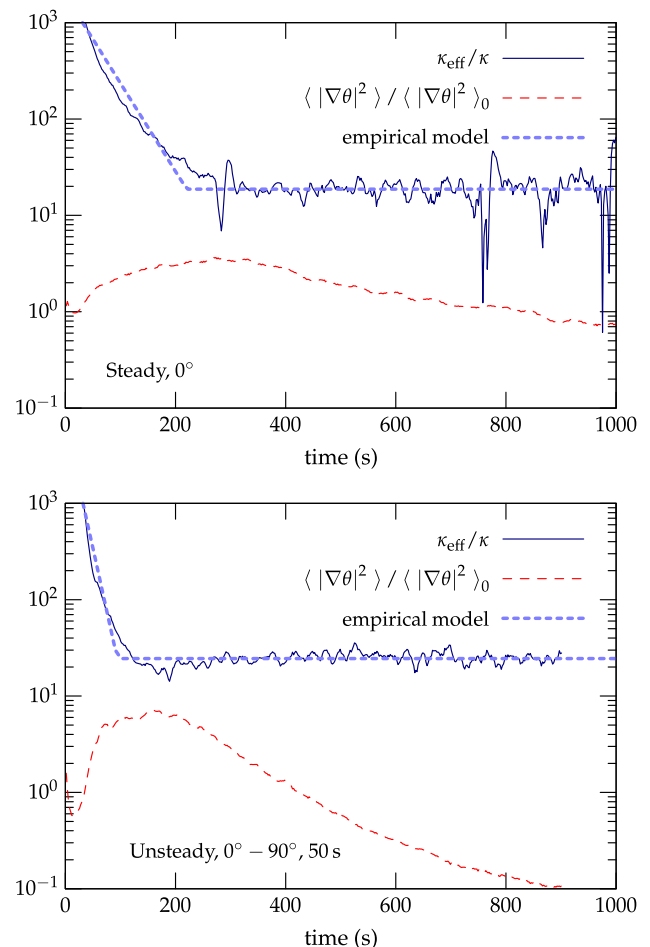
number of realizations providing representative statistics, 65 samples were taken using the flow generated by the magnet angle 0°. The statistics extracted varied in less than 10 % when more than 23 samples were considered. The number of realizations employed in the rest of the experiments was 36. The initial size of the blob of dye was around 50 mm, which is between the square magnet edge and diagonal.

4.3 Effective diffusivity in forced flow

As presented in Sect. 3, a scalar spreading in quiescent brine shows a κ_{eff} different than the one expected in 2D homogeneous diffusion. The discrepancy was attributed solely to the effect of gravity currents. When the fluid is forced, it can be expected that the strained pattern

Fig. 8 Example of scalar statistics for two configurations. $\kappa_{\mathrm{eff}}/\kappa$ and $\langle|\nabla\theta|^2\rangle/\langle|\nabla\theta|^2\rangle_0$ plotted against time for the steady configuration 0° and the unsteady configuration 0°–90° with period 50 s. An empirical model for $\kappa_{\mathrm{eff}}/\kappa$ is also plotted

constant regime, $\kappa_{\mathrm{eff}}^{\infty}$, and the time after which it effectively becomes a constant, t_{κ}^{∞}, are identified. This is done by adjusting a three parameter empirical model to each sample, using a least squares regression. This model, also plotted in Fig. 8, consists of an initially exponential curve continuously followed by a constant. Observation of the statistics presented in Fig. 8 suggests a link between κ_{eff} and the mean gradient squared. This is unexpected in a 2D diffusive system modelled by Eq. 3. Such a link involves one relation between t_{κ}^{∞} and the time for the maximum mean gradient squared and another relation between $\kappa_{\mathrm{eff}}^{\infty}$ and the maximum mean gradient squared, $\langle|\nabla\theta|^2\rangle_{\max}$. A closer study reveals a Pearson's coefficient of up to 0.6 between t_{κ}^{∞} and the time for maximum mean gradient squared, which indicates a strong correlation between these two variables.

The relation between the maximum mean scalar gradient squared and t_{κ}^{∞} is presented in Fig. 9. The top graph presents the cumulative and density distributions of the ratio of $\langle|\nabla\theta|^2\rangle$ at time t_{κ}^{∞} with $\langle|\nabla\theta|^2\rangle_{\max}$. This graph shows how the trend change in κ_{eff} is produced when $\langle|\nabla\theta|^2\rangle$ is relatively close to its maximum: at t_{κ}^{∞}, around 75 % of the samples have a $\langle|\nabla\theta|^2\rangle$ which is at least 75 % of its maximum.

The bottom graph in Fig. 9 presents the relation between $\kappa_{\mathrm{eff}}^{\infty}$ and $\langle|\nabla\theta|^2\rangle_{\max}$. In this case, the behaviour seems to depend on whether the scalar is advected by a quasi-steady or an unsteady flow: quasi-steady flow samples spread along a broader range following what seems to be a power law with an exponent around -0.88. Unsteady experiments show a more compact distribution. Moreover, their $\kappa_{\mathrm{eff}}^{\infty}$ is on average slightly larger for the same maximum mean gradient square.

It is fair to acknowledge that both $\kappa_{\mathrm{eff}}/\kappa$ and $\langle|\nabla\theta|^2\rangle$ may be affected by the acquisition system resolution. The r.m.s. of the strain rate, λ, of the flows employed is smaller than $0.035\,\mathrm{s}^{-1}$. Therefore, those chaotic cases with a $\kappa_{\mathrm{eff}}/\kappa < 15$ are locally unresolved, since their Batchelor length scale $\ell_B \sim \sqrt{\kappa/\lambda}$ is smaller than 1 pix, which leads to measurement saturation (Rossi et al. 2012). This should not affect the conclusions since, on the one hand, in more than 90 % of the points $\kappa_{\mathrm{eff}}/\kappa > 15$ and, on the other hand, the exact value of $\langle|\nabla\theta|^2\rangle$ is not strictly relevant. Nevertheless, this may be the reason why the unsteady configurations, whose smaller scales are around ℓ_B, depart from the trend of the steady ones in the right graph of Fig. 9.

As shown in Fig. 8, $\kappa_{\mathrm{eff}}/\kappa$ has a very high initial value (several thousands) and quickly decreases. Around $t_{|\nabla\theta|^2}^{\max}$, $\kappa_{\mathrm{eff}}/\kappa$ stabilizes around a constant value which ranges between 10 and 100 depending on the maximum mean gradient squared reached in each sample. Although the
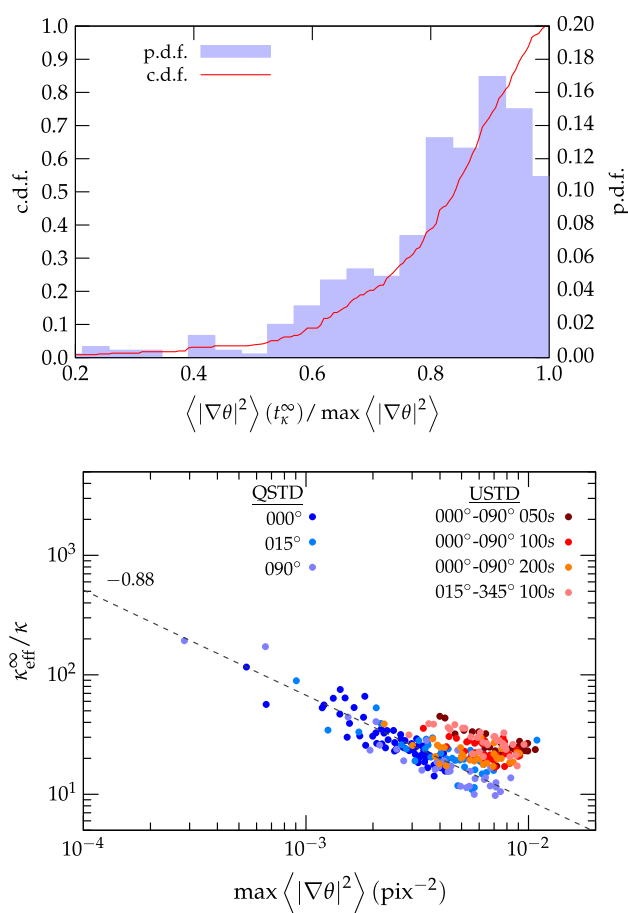

Fig. 9 Relation between $\langle|\nabla\theta|^2\rangle$ and $\kappa_{\mathrm{eff}}/\kappa$. *T*op graph presents the density and cumulative distributions of $\langle|\nabla\theta|^2\rangle$ at t_{κ}^{∞} normalized with its maximum. *B*ottom graph presents the relation between the maximum $\langle|\nabla\theta|^2\rangle$ and $\kappa_{\mathrm{eff}}^{\infty}$ for each configuration

decrease in $\kappa_{\mathrm{eff}}/\kappa$ may seem trivial where $\langle|\nabla\theta|^2\rangle$ increases ($\kappa_{\mathrm{eff}} \propto \langle|\nabla\theta|^2\rangle^{-1}$), for 2D diffusive flows $\kappa_{\mathrm{eff}}/\kappa$ should be 1 regardless of the value of $\langle|\nabla\theta|^2\rangle$. Also, the increment of $\langle|\nabla\theta|^2\rangle$ is several orders of magnitude smaller than the decrement of κ_{eff}. In fact, configurations with nearly constant $\langle|\nabla\theta|^2\rangle$ still display the two regimes in $\kappa_{\mathrm{eff}}/\kappa$.

The graphs in Fig. 10 present the sample average of $\kappa_{\mathrm{eff}}/\kappa$ for the configurations tested. In these, it can be observed that after t_{κ}^{∞}, κ_{eff} still moderately depends on the flow. This is evidenced by the low frequency oscillation in the configuration 000°–090°, 200 s, after 300 s. The period of this oscillation coincides with that employed for the body forcing. Also, $\kappa_{\mathrm{eff}}/\kappa$ presents a higher value in the half period with magnets at 000°, and a lower value when the magnets are at 090°, qualitatively matching the relations observed in the steady cases (top graph).

A possible phenomenology behind the behaviour observed is that the initial decay of κ_{eff} is produced by
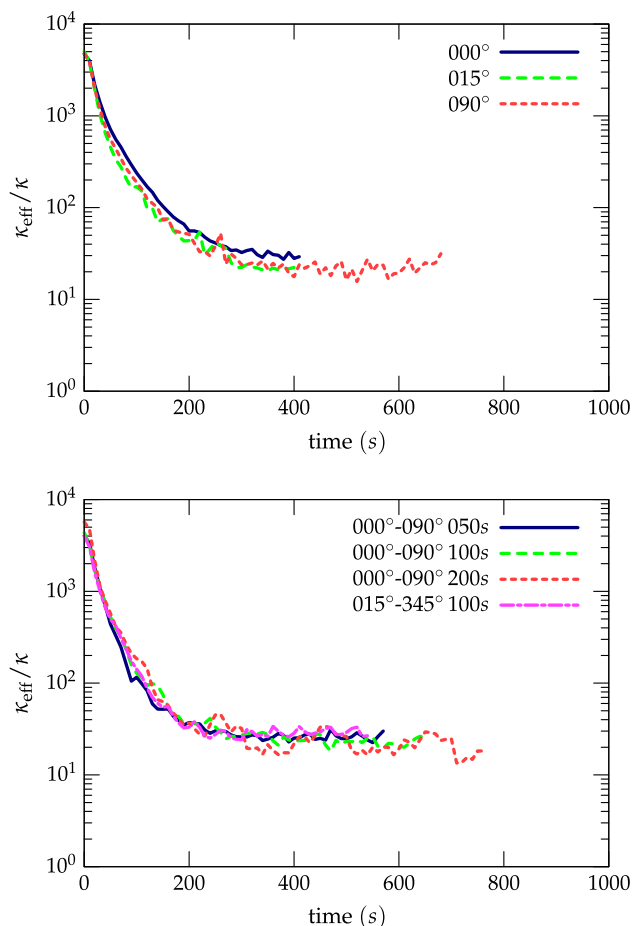
Fig. 10 Average of $\kappa_{\text{eff}}/\kappa$. Averages for the different samples grouped by configurations

gravity currents while the constant regime comes from vertical velocity gradients and free surface divergence. At short times, gradient production accelerates the gravitational spreading reducing the vertical thickness of the scalar. At the same time, the flow redistributes the scalar over an increasing area, A_t.

Well before $t^{\max}_{|\nabla\theta|^2}$, A_t drastically reduces its spreading in steady (where the scalar wraps around a vortex) and unsteady flows (whose chaotic area is restricted to the central forced zone). From this moment, the scalar mainly fills A_t as $\langle|\nabla\theta|^2\rangle$ increases. As this occurs, the gravity currents lose strength since consecutive scalar stripes interact with each other when they become closer. At t^{∞}_{κ} the weakened gravity currents are overcome by the dispersion produced by vertical velocity gradients and free surface divergence.

As A_t is filled, the gradient increment is also curbed, since the blurring of consecutive stripes affect each other, and therefore, $\langle|\nabla\theta|^2\rangle$ saturates, reaching a maximum. The times $t^{\max}_{|\nabla\theta|^2}$ and t^{∞}_{κ} are therefore correlated by the time which takes the scalar to fill A_t.

The maximum $\langle|\nabla\theta|^2\rangle$ reached will be higher the larger A_t is, because there is more space to be filled before the gradient saturation. Also, the larger the A_t the thinner is the scalar vertical dimension. This accounts for the inverse correlation between maximum $\langle|\nabla\theta|^2\rangle$ and $\kappa_{\text{eff}}^{\infty}$: vertical velocity gradients would disperse scalar faster, the thicker is its vertical dimension.

In addition, the variance decay rate produced vertical velocity gradients and free surface divergence is also proportional to $\langle|\nabla\theta|^2\rangle$ and controlled by the particular 3D velocity field. This could explain the nearly constant, but still slightly dependent on the flow, value of κ_{eff}.

5 Conclusions

In this paper, we have presented a method for evaluating the errors arising from the assumption of two-dimensionality in free surface scalar experiments.

To obtain the required accuracy in the statistics, in Sect. 2, we performed a calibration of the acquisition system which included the use of double picture estimators. The expected value of such estimators is independent on the ASN and approaches to the real scalar statistic as the time between the two pictures, T, is reduced. These estimators solve at least all the length scales down to $\ell \sim UT$, where U is a characteristic velocity of the flow.

It was observed that, in addition to diffusivity, three mechanisms contribute to the 2D variance decay. These are the vertical velocity gradients, the free surface divergence and the scalar-induced gravity currents. Although these phenomena also produce scalar energy transfer across the spectrum, if $Pe \gg 1$ their effect is small when compared with advection and they were only evaluated against diffusion.

The particular effect of gravity currents was evidenced in Sect. 3 for a scalar spreading in homogeneous or stratified quiescent brine: gravity currents produced a variance decay several orders of magnitude larger than diffusion. In forced flows, we hypothesized in Sect. 4 that gravity currents only dominate the initial variance decay, typically lasting between 100 and 300 s for the presented apparatus, and that the subsequent 2D homogenization is mainly produced by vertical velocity gradients and free surface divergence. This second regime is characterized by a ratio between 2D variance decay and 2D mean gradient squared, called κ_{eff}, almost constant in time, between 10 and 100 times larger than the expected 2D diffusion and slightly dependent on the velocity field.

Independently on the exact phenomena behind the evolution of κ_{eff}, two conclusions can be drawn by observing the data acquired. Firstly, despite the great care

taken for the calibration and experimental procedure, κ_{eff}/κ is always considerably larger than 1; in consequence, we do not capture the strictly 2D transport equation of a passive scalar. Secondly, in forced flows, the strong time dependence of κ_{eff} seems to vanish after t_κ^∞, remaining only a weaker dependence with the velocity field. Taking this into account, the nearly constant κ_{eff} makes it possible to qualitatively study some aspects of mixing in such Q2D flows, while it may contribute to explain some discrepancies with theory, observed in past experimental works dealing with 2D scalar mixing.

References

Amen R, Maxworthy T (1980) The gravitational collapse of a mixed region into a linearly stratified fluid. J Fluid Mech 96:65–80

Axelrod D, Koppel DE, Schlessinger J, Elson E, Webb WW (1976) Mobility measurement by analysis of fluorescence photobleaching recovery kinetics. Biophys J 16:1055–1069

Cenedesse C, Dalziel S (1998) Concentration and depth fields determined by the light transmitted through a dyed solution. In: Carlomagno GM, Grant I (eds) 8th international symposium on flow visualization, Sorrento, Italy, pp 61.1–61.5

Fay JA (1969) The spread of oil slicks on a Calm Sea. Plenum Press, New York

Fay JA (1971) Physical processes in the spread of oil on a water surface. In: A. P. Institute (ed) Proceedings of the joint conference on the prevention and control of oil spills, Washington, DC, pp 463–467

Garcia de la Cruz JM (2011) Experimental study of free surface mixing in vortical and chaotic flows. Ph.D. thesis, Imperial College, London

Gouillart E, Dauchot O, Thiffeault JL, Roux S (2009) Open-flow mixing: experimental evidence for strange eigenmodes. Phys Fluids 21:023603

Guilbault GG (1973) Practical fluorescence, 2nd edn. Marcel Dekker, New York

Hoult DP (1972) Oil spreading on the sea. Annu Rev Fluid Mech 4:341–368

Jana SC, Tjahjadi M, Ottino JM (1994) Chaotic mixing of viscous fluids by periodic changes in geometry: baffled cavity flow. Anal Chem E 40:1769–1781

Jullien MC (2003) Dispersion of passive tracers in the direct enstrophy cascade: experimental observations. Phys Fluids 15:2228–2237

Jullien MC, Castiglione P, Tabeling P (2000) Experimental observation of batchelor dispersion of passive tracers. Phys Rev Lett 85:3636–3639

Raffel M, Willert C, Wereley S, Kompenhans J (1998) Particle image velocimetry. Springer, Berlin

Rossi L, Bocquet S, Ferrari S, Garcia de la Cruz JM, Lardeau S (2009) Control of flow geometry using electromagnetic body forcing. Int J Heat Fluid Flow 30:505–513

Rossi L, Doorly D, Kustrin D (2012) Lamination and mixing in laminar flows driven by Lorentz body forces. Europhys Lett 97:14006

Rossi L, Vassilicos JC, Hardalupas Y (2006) Electromagnetically controlled multi-scale flows. J Fluid Mech 558:207–241

Rothstein D, Henry E, Gollub JP (1999) Persistent patterns in transient chaotic fluid mixing. Nature 401:770–772

Ungarish M, Huppert HE (2004) On gravity currents propagating at the base of a stratified ambient: effects of geometrical constraints and rotation. J Fluid Mech 521:69–104

Voth GA, Haller G, Gollub JP (2002) Experimental measurements of stretching fields in fluid mixing. Phys Rev Lett 88:254501

Voth GA, Saint TC, Dobler G, Gollub JP (2003) Mixing rates and symmetry breaking in two-dimensional chaotic flow. Phys Fluids 15:2560–2566

Warhaft Z (2000) Passive scalars in turbulent flows. Annu Rev Fluid Mech 32:203–240

Weast RC (1989) Handbook of chemistry and physics: a ready-reference book of chemical and physical data, 70th edn. CRC Press, Boca Raton

Williams BS, Marteau D, Gollub JP (1997) Mixing of a passive scalar in magnetically forced two-dimensional turbulence. Phys Fluids 9:2061–2080

Wolf AV (1966) Aqueous solutions and body fluids. Harper and Row, New York

Wu J (1969) Mixed region collapse with internal wave generation in a density-stratified medium. J Fluid Mech 35:531–544